EXPERIMENTAL AND NUMERICAL STUDIES ON UTILIZATION OF SOME INDUSTRIAL WASTES IN FLEXIBLE ROAD PAVEMENTS

SATYAJIT PATEL

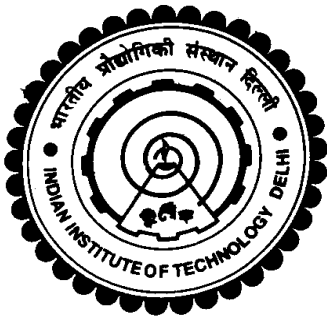

DEPARTMENT OF CIVIL ENGINEERING
INDIAN INSTITUTE OF TECHNOLOGY DELHI
DECEMBER 2016

EXPERIMENTAL AND NUMERICAL STUDIES ON UTILIZATION OF SOME INDUSTRIAL WASTES IN FLEXIBLE ROAD PAVEMENTS

by

SATYAJIT PATEL

Department of Civil Engineering

Submitted

in fulfilment of the requirements of the degree of *Doctor of Philosophy*

to the

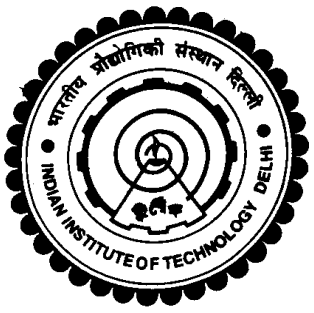

INDIAN INSTITUTE OF TECHNOLOGY DELHI

DECEMBER 2016

CERTIFICATE

This is to certify that the thesis entitled "**EXPERIMENTAL AND NUMERICAL STUDIES ON UTILIZATION OF SOME INDUSTRIAL WASTES IN FLEXIBLE ROAD PAVEMENTS"** being submitted by **Mr. Satyajit Patel** to the **Indian Institute of Technology Delhi** is a record of bonafide research work carried out by him under my supervision and guidance. The thesis work, in our opinion, has reached the standard, fulfilling the requirements for **DOCTOR OF PHILOSOPHY** degree. The research report and results presented in this thesis have not been submitted, in part or full, to any University or Institute for the award of any degree or diploma.

New Delhi
December, 2016

Dr. J. T.Shahu
Professor
Civil Engineering Department
Indian Institute of Technology Delhi

ACKNOWLEDGEMENTS

On the completion of this work, it is my pride and privilege to express my deepest gratitude with great appreciation to my supervisor, Dr. J. T. Shahu for his irreplaceable encouragement, inspiring guidance, keen interest, unfailing support and constant encouragement throughout this study. A person of myriad skills, he eased the way of my work by his wonderful contribution. His volunteered hours of valuable time helped me to put my best foot forward in right direction. His vast knowledge and experience on the subject made this study possible and even, more enjoyable.

My sincere thanks to Prof. K. G. Sharma, Prof. K. C. Iyer, Prof. Puneet Mahajan and all faculty members in the Civil Engineering Department for providing me with constant encouragement and valuable suggestions. I also thank Dr. C. H. Solanki, Professor, Applied Mechanics Department, SVNIT, Surat.

I am thankful to soil mechanics laboratory staff at IIT Delhi and SVNIT, Surat.

My special thanks to all my friends Mr. Kausar Ali, Mrs. Sowmiya, Dr. Ramana Reddy, Mr. Suresh Kumar, Dr. Shantanu Patra, Dr. Shailendra Kumar and Mr. Jignesh B. Patel.

Last, but certainly not the least, words alone cannot express my deepest gratitude for the constant support, understanding and affection that I received from my parents and my family members during the tenure of this study that provided me the necessary impetus to work on this thesis.

Satyajit Patel

ABSTRACT

Development of adequate road network is very important for the socio-economic development of a country. For construction, maintenance and widening of roads, a large quantum of construction material is required. Consequently, there is a scarcity of suitable conventional materials for construction of subbase and base layers of flexible pavements. Besides, the cost of extracting good quality of natural material is also increasing. On the other hand, due to rapid economic growth and industrialization, a large quantity of waste materials such as electric arc furnace steel slag, copper slag, blast furnace slag, granulated blast furnace slag and fly ash is being generated creating a threat to public health and ecology.

In recent years, there has been a growing emphasis and interest all over the world towards promoting the use of marginal materials in road construction in order to affect cost saving, reduce pressure on good quality aggregates and also to protect environment. This research work proposes the bulk utilization of these industrial solid wastes in the area of road construction which will help reduce the gap between their generation and utilization and also reduce the requirement of precious conventional aggregates.

The scope of the present research consists of two main parts, namely, experimental investigations on engineering properties of different waste material and three-dimensional finite element analysis of five layer flexible pavement system. The experimental program is carried out in two parts. First, compaction characteristics, unconfined compressive strength, CBR, resilient modulus and cumulative plastic strain of different trial mixes of the waste materials are investigated and the optimum mixes are determined. Next, durability tests, unconsolidated undrained triaxial tests, X-ray diffraction (XRD) tests, scanning electron microscopy (SEM) tests and pavement model tests are performed on the optimum mixes. The tests are carried out on different combinations of copper slag-fly ash-dolime (CFD) mix, fine steel slag-fly ash-dolime (FSFD) mix, coarse steel slag-fly ash-dolime (CSFD) mix, blast furnace slag-fly ash-dolime (BFD) mix, copper slag-fly ash (CF) mix, granulated blast furnace slag-fly ash (GBF) mix, fly

ash-dolime (FD) mix and Black Cotton soil-dolime (BCD) mix. The CFD, FSFD, CSFD and BFD mixes are candidate mixes for the utilization in the base course of flexible pavement system, whereas CF, GBF, FD and BCD are candidate mixes for the subbase course. These mixes were chosen based on their strength characteristics and availability of those particular waste materials in the vicinity of the corresponding metal industry. The behaviour of the these waste mixes for base course are compared with that of the conventional Wet Mix Macadam (WMM) and the waste mixes for subbase course are compared with that of the conventional Granular Subbase (GSB).

Based on the engineering properties obtained for the different trial mixes of the proposed base materials the following four optimum mix proportions were adopted as per the strength requirements of Indian Road Congress:

i. 69.6% copper slag + 17.4% fly ash + 13% dolime mix
ii. 65.3% fine steel slag + 21.7% fly ash + 13% dolime mix
iii. 77.8% coarse steel slag + 13.3% fly ash + 8.9% dolime mix
iv. 71.4% blast furnace slag + 15.9% fly ash + 12.7% dolime mix

Similarly, the following four optimum mix proportions were adopted for subbase course:

i. Black Cotton soil + 9% dolime mix
ii. Fly ash + 10% dolime mix
iii. 70% copper slag + 30% fly ash mix
iv. 10% granulated blast furnace slag + 90% fly ash mix

All the four optimum base mixes give better performance compared to WMM in terms of strength, elastic modulus, resilient modulus, permanent strain and load-settlement relationship in pavement model test. Elastic modulus and resilient modulus of GSB were found to be lower than that of BCD mix and FD mix, and higher than that of CF mix and GBF mix. The values of deviator stress at failure for the optimum subbase mixes were found to be higher compared to that of GSB. Among the three stress-dependent models of resilient modulus, the three-parameter

model (Model 3) provided the best fit. A logarithmic model provided a very good fit regression equation for the estimation of permanent strain.

The service life of a flexible pavement having the optimum mixes in the base course vis-a-vis the conventional Wet Mix Macadam (WMM) base layer and optimum mixes in the subbase course vis-a-vis the conventional Granular Subbase (GSB) layer is also evaluated in the present study through finite-element analyses of a five layer flexible pavement system. The service life of the pavement with optimum mixes as the base course is higher than that of the pavement with WMM as base course as per fatigue failure criterion, whereas this value is lower as per rutting failure criterion. The equivalent thicknesses of optimum mixes base as obtained by fatigue failure criterion are close to those obtained by AASHTO method and triaxial test method.

CONTENTS

			Page no.
1	**Introduction**		**1**
	1.1	General	1
	1.2	Types of waste materials used	3
		1.2.1 Copper slag	4
		1.2.2 Steel slag	6
		1.2.3 Blast furnace slag	9
		1.2.4 Fly ash	10
		1.2.5 Dolime	11
	1.3	Objectives	12
	1.4	Methodology	13
		1.4.1 Laboratory tests	13
		1.4.2 Model tests	14
		1.4.3 Numerical analysis	15
	1.5	Need of present study	15
		1.5.1 Laboratory tests	16
		1.5.2 Model tests	17
		1.5.3 Numerical analysis	17
	1.6	Organization of the thesis	18

2 Literature Review **21**

2.1 Properties of copper slag and its utilization 21

2.2 Properties of steel slag and its utilization 26

2.3 Properties of blast furnace slag and its utilization 31

2.4 Properties of stabilized expansive soil and its utilization 37

2.5 Dynamic behaviour of conventional and waste materials 43

2.6 Research gaps 56

3 Experimental Investigations **59**

3.1 Raw materials 59

3.2 Experimental program 60

3.2.1 Physical and chemical properties 60

3.2.2 Mix proportions and compaction characteristics 60

3.2.3 Unconfined compressive strength 62

3.2.4 CBR 63

3.2.5 Cyclic load triaxial tests 63

3.2.6 Durability tests 65

3.2.7 Expansion tests 66

3.2.8 Monotonic triaxial tests 66

3.2.9 X-ray diffraction and scanning electron microscopy tests 68

3.2.10 Model tests 69

4 Finite Element Analysis **71**

4.1 General 71

4.2 Finite element method 72

4.3	Plaxis software		72
4.4	Finite element model		73
	4.4.1	Model description	73
	4.4.2	Model boundaries	74
	4.4.3	Validation of finite element results	76
5	**Results and Discussion for Base Materials**		**77**
5.1	Physical and chemical properties of raw materials		77
5.2	Base Material I – Copper slag – Fly ash- Dolime – (CFD) Mix		81
	5.2.1	Compaction characteristics	81
	5.2.2	Unconfined compressive strength	83
	5.2.3	Resilient modulus	92
	5.2.4	Modeling of resilient modulus response	95
	5.2.5	Permanent strain characteristics	101
	5.2.6	Durability characteristics	106
	5.2.7	Monotonic triaxial tests	106
	5.2.8	Correlation of deviator stress at failure and cohesion with UCS values	110
	5.2.9	X-ray diffraction analysis	111
	5.2.10	SEM observations	114
5.3	Base material II – Fine steel slag-Fly ash- Dolime (FSFD) Mix		116
	5.3.1	Compaction characteristics	116
	5.3.2	Unconfined compressive strength	118
	5.3.3	Resilient modulus	123

	5.3.4	Modeling of resilient modulus response	125
	5.3.5	Permanent strain characteristics	129
	5.3.6	Durability characteristics	132
	5.3.7	Monotonic triaxial tests	133
	5.3.8	Correlation of deviator stress at failure and cohesion with UCS values	135
	5.3.9	X-ray diffraction analysis	136
	5.3.10	SEM observations	138
5.4	Base Material III – Coarse steel slag – Fly ash – Dolime (CSFD) mix		140
	5.4.1	Compaction characteristics	140
	5.4.2	Unconfined compressive strength	141
	5.4.3	Resilient modulus	143
	5.4.4	Modeling of resilient modulus response	146
	5.4.5	Permanent strain characteristics	149
	5.4.6	Durability characteristics	152
	5.4.7	Monotonic triaxial tests	153
	5.4.8	Correlation of deviator stress at failure and cohesion with UCS values	155
	5.4.9	X-ray diffraction analysis	156
	5.4.10	SEM observations	158
5.5	Base Material IV – Blast furnace slag – Fly ash – Dolime (BFD) Mix		159
	5.5.1	Compaction characteristics	159
	5.5.2	Unconfined compressive strength	160

5.5.3 Resilient modulus 162

5.5.4 Modeling of resilient modulus response 165

5.5.5 Permanent strain characteristics 168

5.5.6 Durability characteristics 170

5.5.7 Monotonic triaxial tests 171

5.5.8 Correlation of deviator stress at failure and cohesion with UCS values 174

5.5.9 X-ray diffraction analysis 175

5.5.10 SEM observations 177

6 Results and Discussion for Subbase Materials 179

6.1 Physical and chemical properties of raw materials 179

6.2 Subbase Material I – Black Cotton Soil – Dolime (BCD) mix 183

6.2.1 Atterberg limit 183

6.2.2 Free swell index 184

6.2.3 Compaction characteristics 184

6.2.4 Unconfined compressive strength 184

6.2.5 California bearing ratio (CBR) 187

6.2.6 Resilient modulus 188

6.2.7 Modeling of resilient modulus response 190

6.2.8 Permanent strain characteristics 193

6.2.9 Monotonic triaxial tests 196

6.2.10 Correlation of deviator stress at failure and cohesion with UCS values 198

6.2.11 X-ray diffraction analysis 200

	6.2.12	SEM observations	201
6.3		Subbase Material II – Fly ash – Dolime (FD) mix	202
	6.3.1	Compaction characteristics	202
	6.3.2	Unconfined compressive strength	203
	6.3.3	California bearing ratio (CBR)	205
	6.3.4	Resilient modulus	205
	6.3.5	Modeling of resilient modulus response	207
	6.3.6	Permanent strain characteristics	210
	6.3.7	Durability characteristics	212
	6.3.8	Monotonic triaxial tests	213
	6.3.9	Correlation of deviator stress at failure and cohesion with UCS values	215
	6.3.10	X-ray diffraction analysis	217
	6.3.11	SEM observations	218
6.4		Subbase Material III – Copper slag – Fly ash (CF) mix	219
	6.4.1	Compaction characteristics	219
	6.4.2	Unconfined compressive strength	219
	6.4.3	California bearing ratio (CBR)	221
	6.4.4	Resilient modulus	222
	6.4.5	Modeling of resilient modulus response	224
	6.4.6	Permanent strain characteristics	227
	6.4.7	Monotonic triaxial tests	229
	6.4.8	Correlation of deviator stress at failure and cohesion with UCS values	232

6.4.9 X-ray diffraction analysis 233

6.4.10 SEM observations 233

6.5 Subbase Material IV – Granulated Blast Furnace slag – Fly ash (GBF) mix 235

6.5.1 Compaction characteristics 235

6.5.2 California bearing ratio (CBR) 235

6.5.3 Unconfined compressive strength 237

6.5.4 Resilient modulus 237

6.5.5 Modeling of resilient modulus response 240

6.5.6 Permanent strain characteristics 242

6.5.7 Monotonic triaxial tests 244

6.5.8 Correlation of deviator stress at failure and cohesion with UCS values 247

6.5.9 X-ray diffraction analysis 249

6.5.10 SEM observations 250

7 Comparison of Base Materials and Subbase Materials 251

7.1 Base materials 251

7.1.1 Compaction characteristics 252

7.1.2 Unconfined compressive strength 253

7.1.3 Triaxial shear strength 255

7.1.4 Resilient modulus 257

7.1.5 Modeling of resilient modulus response 259

7.1.6 Permanent strain characteristics 261

7.1.7 Model tests 263

7.1.8 Service life of flexible pavements 264
7.1.9 Equivalent thickness of optimum mix base layers 270
7.2 Subbase materials 273
7.2.1 Compaction characteristics 273
7.2.2 Unconfined compressive strength 274
7.2.3 Triaxial shear strength 276
7.2.4 Resilient modulus 278
7.2.5 Modeling of resilient modulus response 280
7.2.6 Permanent strain characteristics 282
7.2.7 Model tests 284
7.2.8 Service life of flexible pavements 285
7.2.9 Equivalent thickness of optimum mix base layers 291
8 Conclusions and Suggestions for Future Research 295
8.1 General 295
8.2 Conclusions from base materials 296
8.2.1 Conclusions for CFD mix 296
8.2.2 Conclusions for other industrial waste mixes 298
8.2.3 Comparison of all base waste mixes 299
8.3 Conclusions from Subbase materials 301
8.3.1 Conclusions for individual waste mixes 301
8.3.2 Comparison of all subbase waste mixes 303
8.4 Suggestions for future research 305
References 307

List of Figures

Figure no.	Description	Page no.
Fig. 1.1	Types of slag	4
Fig. 1.2	Photographs of copper slag	5
Fig. 1.3	Year wise copper production in India	5
Fig. 1.4	Photographs of steel slag	8
Fig. 1.5	Year wise production of crude steel in India	8
Fig. 1.6	Photographs of blast furnace slag and GBFS	10
Fig. 1.7	Photographs of fly ash and Dolime	12
Fig. 2.1	Angle of friction of copper slag at varying relative densities	23
Fig. 2.2	Variation of MDD and OMC with copper slag content	24
Fig. 2.3	Variation of soaked CBR with copper slag content	24
Fig. 2.4	Typical pavement cross section for a two-lane highway	25
Fig. 2.5	Variation of UCS with BF Slag content for 28 days curing	37
Fig. 2.6	Variation of UCS with curing period for 10% fly ash + 90% BF Slag mix	37
Fig. 2.7	Variation of Atterberg limits with content of unslaked lime.	40
Fig. 2.8	Effect of lime on plasticity characteristics	42
Fig. 2.9	Effect of lime on free swell index	42
Fig. 2.10	Effect of lime on CBR value	42
Fig. 2.11	Effect of lime on unconfined compression strength	42
Fig. 2.12	Strains in granular materials during one cycle of load application	44
Fig. 2.13	Resilient modulus versus confining stress	48
Fig. 2.14	Resilient moduli of DGS and conventional base aggregates.	48
Fig. 2.15	Effect of confinement on static modulus	50

Fig. 2.16	Variation of resilient strains with number of cycles	51
Fig. 2.17	Variation of permanent strains with number of cycles	51
Fig. 2.18	Variation of resilient modulus with number of load cycles	52
Fig. 2.19	Resilient modulus of treated and untreated soils	53
Fig. 2.20	Resilient strain at deviator stress of 68 kPa and cell pressure of 40 kPa	54
Fig. 2.21	Permanent strain at deviator stress of 68 kPa and cell pressure of 40 kPa	55
Fig. 2.22	Resilient modulus at deviator stress of 68 kPa and cell pressure of 40 kPa	55
Fig. 3.1	Cyclic load triaxial (CLT) test setup used in this study	65
Fig. 3.2	Photographs of various tests under progress	67
Fig. 3.3	Photograph of XRD test equipment	68
Fig. 3.4	Photograph of SEM test equipment	69
Fig. 3.5	Schematic diagram of the pavement model test	70
Fig. 4.1	Finite-element analysis of flexible pavement system using code Plaxis 3D for traffic intensity of 100 msa and subgrade CBR of 4%	73
Fig. 4.2	Variation of vertical compressive strain at the top of subgrade with thickness of subgrade layer	75
Fig. 4.3	Variation of vertical compressive strain at the top of subgrade with lateral dimension of the model	75
Fig. 4.4	Comparison of load-settlement curves of model test and finite element analysis	76
Fig. 5.1	Grain size distribution curves of raw materials	79
Fig. 5.2	Modified Proctor compaction curves for various copper slag-fly ash mixes	82
Fig. 5.3	Modified Proctor compaction curves for 70% copper slag-30% fly ash mix with varying dolime content	83

Fig. 5.4	Variation of maximum dry unit weight with optimum moisture content for different copper slag-fly ash-dolime mixes	84
Fig. 5.5	Variation of UCS with fly ash content for 28 days of curing	85
Fig. 5.6	Particle size distribution of copper slag-fly ash mixes	86
Fig. 5.7	Variation of UCS with dolime content for 28 days of curing	87
Fig. 5.8	Variation of UCS with curing period for 15% Dolime	88
Fig. 5.9	Variation of UCS with curing period for 20% fly ash	89
Fig. 5.10	Relationship between UCS and curing period for different stabilized materials	90
Fig. 5.11	Measured UCS versus predicted UCS using power model for 64 CFD mixes	91
Fig. 5.12	Influence of deviatoric and confining stresses on resilient modulus of optimum CFD mix at 28 days curing	93
Fig. 5.13	Variation of resilient modulus with fly ash and dolime contents (cell pressure = 34.5 kPa, deviator stress = 93.1 kPa and curing period = 28 days)	94
Fig. 5.14	Effect of curing period on resilient modulus versus deviator stress relationship for optimum CFD mix and Wet Mix Macadam (WMM) at a constant cell pressure of 34.5 kPa.	95
Fig. 5.15	Effect of dolime content on resilient modulus versus deviator stress relationship for 20% fly ash content and 28 days curing period.	97
Fig. 5.16	Effect of dolime content on resilient modulus versus bulk stress relationship for 20% fly ash content and 28 days curing period	97
Fig. 5.17	Measured resilient modulus versus predicted resilient modulus using $M_r - \sigma_d$ model for 19 CFD mixes.	99
Fig. 5.18	Measured resilient modulus versus predicted resilient modulus using M_r - θ model for 19 CFD mixes	100
Fig. 5.19	Measured resilient modulus versus predicted resilient modulus using three parameter model for 19 CFD mixes.	100
Fig. 5.20	Deviator stress versus axial strain relationship during conditioning	102

phase for optimum CFD mix.

Fig. 5.21 Effect of curing period on permanent strain versus loading cycle relationship for optimum CFD mix and conventional Wet Mix Macadam (WMM). 102

Fig. 5.22 Variation of permanent strain after 10000 cycles with fly ash and dolime contents for 28 days of curing period 103

Fig. 5.23 Measured plastic strain versus predicted plastic strain using logarithmic model for 19 CFD mixes. 105

Fig. 5.24 Relationship between deviator stress at failure and cell pressure for different curing periods 107

Fig. 5.25 Relationship between elastic modulus and cell pressure for different curing periods 108

Fig. 5.26 Modified failure envelopes at various curing periods for the optimum mix(80C-20F-15D) 109

Fig. 5.27 Relationship between deviator stress at failure and UCS 110

Fig. 5.28 Relationship between cohesion and UCS 111

Fig. 5.29 Scanning electron microscopy images of hydrated products of copper slag-fly ash-dolime mixes for 1 day and 28 days curing period 115

Fig. 5.30 Proctor compaction curves for various fine steel slag-fly ash mixes 117

Fig. 5.31 Modified Proctor compaction curves for 85% fine steel slag-15% fly ash mix with varying dolime content 117

Fig. 5.32 Variation of maximum dry unit weight with optimum moisture content for different fine steel slag-fly ash-dolime mixes 118

Fig. 5.33 Variation of UCS with fly ash content for 28 days of curing 119

Fig. 5.34 Variation of UCS with dolime content for 28 days of curing 119

Fig. 5.35 Particle size distribution of fine steel slag-fly ash mixes 120

Fig. 5.36 Variation of UCS with curing period for 15% dolime content 121

Fig. 5.37 Variation of UCS with curing period for 25% fly ash content 121

Fig. 5.38	Measured UCS versus predicted UCS using power model for 64 FSFD mixes	123
Fig. 5.39	Influence of deviatoric and confining stresses on resilient modulus of optimum FSFD mix at 28 days curing	124
Fig. 5.40	Variation of resilient modulus with fly ash and dolime contents (cell pressure = 34.5 kPa, deviator stress = 93.1 kPa and curing period = 28 days)	124
Fig. 5.41	Effect of curing period on resilient modulus versus deviator stress relationship for optimum FSFD mix and Wet Mix Macadam (WMM) at a constant cell pressure of 34.5 kPa.	125
Fig. 5.42	Measured resilient modulus versus predicted resilient modulus using $M_r - \sigma_d$ model for 19 FSFD mixes	127
Fig. 5.43	Measured resilient modulus versus predicted resilient modulus using M_r - θ model for 19 FSFD mixes	128
Fig. 5.44	Measured resilient modulus versus predicted resilient modulus using three parameter model for 19 FSFD mixes.	128
Fig. 5.45	Effect of curing period on permanent strain versus loading cycle relationship for optimum FSFD mix and conventional WMM	129
Fig. 5.46	Variation of permanent strain after 10000 cycles with fly ash and dolime contents for 28 days of curing period.	130
Fig. 5.47	Measured plastic strain versus predicted plastic strain using logarithmic model for 19 FSFD mixes.	132
Fig. 5.48	Relationship between deviator stress at failure and cell pressure for different curing periods	133
Fig. 5.49	Relationship between elastic modulus and cell pressure for different curing periods	134
Fig. 5.50	Modified failure envelopes at various curing periods for the optimum mix (75S-25F-15D)	134
Fig. 5.51	Relationship between deviator stress at failure and UCS	135
Fig. 5.52	Relationship between cohesion and UCS	136
Fig. 5.53	Scanning electron microscopy images of hydrated products of fine	139

steel slag-fly ash-dlime mixes for 1 day and 28 days curing period

Fig. 5.54 Modified Proctor compaction curves for various coarse steel slag-fly ash-dolime mixes. 141

Fig. 5.55 Unconfined compressive strength (UCS) of various coarse steel slag-fly ash-dolime mixes (Mix 1 – Mix 5: 28 days curing, Mix 6: 0, 7, 14 and 28 days curing). 142

Fig. 5.56 Particle size distribution of coarse steel slag-fly ash-dolime mixes 143

Fig. 5.57 Influence of deviatoric and confining stresses on resilient modulus of optimum CSFD mix at 28 days curing 144

Fig. 5.58 Influence of aggregate/binder ratio and fly ash/dolime ratio on resilient modulus of CSFD mix (cell pressure = 34.5 kPa and curing period = 28 days) 145

Fig. 5.59 Effect of curing period on resilient modulus versus deviator stress relationship for optimum CSFD mix and Wet Mix Macadam (WMM) at a constant cell pressure of 34.5 kPa. 146

Fig. 5.60 Measured resilient modulus versus predicted resilient modulus using $M_r - \sigma_d$model for 9 CSFD mixes 148

Fig. 5.61 Measured resilient modulus versus predicted resilient modulus using M_r - θ model for 9 CSFD mixes 148

Fig. 5.62 Measured resilient modulus versus predicted resilient modulus using three parameter model for 9 CSFD mixes 149

Fig. 5.63 Effect of curing period on permanent strain versus loading cycle relationship for optimum CSFD mix and conventional WMM. 150

Fig. 5.64 Permanent strain of trial mixes after 10000 cycles for 28 days of curing period. 150

Fig. 5.65 Measured plastic strain versus predicted plastic strain using logarithmic model for 9 CSFD mixes. 152

Fig. 5.66 Relationship between deviator stress at failure and cell pressure for different curing periods 153

Fig. 5.67 Relationship between elastic modulus and cell pressure for different curing periods 154

Fig. 5.68	Modified failure envelopes at various curing periods for the optimum CSFD mix	154
Fig. 5.69	Relationship between deviator stress at failure and UCS	155
Fig. 5.70	Relationship between cohesion and UCS	156
Fig. 5.71	Scanning electron microscopy images of hydrated products of coarse steel slag-fly ash-dolime mixes for 1 day and 28 days of curing period	158
Fig. 5.72	Modified Proctor compaction curves for various blast furnace slag-fly ash-dolime mixes.	160
Fig. 5.73	Unconfined compressive strength (UCS) of various blast furnace slag-fly ash-dolime mixes (Mix 1: 0, 7, 14 and 28 days curing, Mix 2 – Mix 6: 28 days curing).	161
Fig. 5.74	Particle size distribution of blast furnace slag-fly ash-dolime mixes	162
Fig. 5.75	Influence of deviatoric and confining stresses on resilient modulus of optimum BFD mix at 28 days curing	163
Fig. 5.76	Influence of aggregate/binder ratio and fly ash/dolime ratio on resilient modulus of BFD mix (cell pressure = 34.5 kPa and curing period = 28 days)	163
Fig. 5.77	Effect of curing period on resilient modulus versus deviator stress relationship for optimum BFD mix and Wet Mix Macadam (WMM) at a constant cell pressure of 34.5 kPa.	164
Fig. 5.78	Measured resilient modulus versus predicted resilient modulus using $M_r - \sigma_d$model for 9 BFD mixes.	166
Fig. 5.79	Measured resilient modulus versus predicted resilient modulus using M_r - θ model for 9 BFD mixes.	167
Fig. 5.80	Measured resilient modulus versus predicted resilient modulus using three parameter model for 9 BFD mixes	167
Fig. 5.81	Effect of curing period on permanent strain versus loading cycle relationship for optimum BFD mix and conventional WMM.	168
Fig. 5.82	Permanent strain of trial mixes after 10000 cycles for 28 days of curing period.	169

Fig. 5.83	Measured plastic strain versus predicted plastic strain using logarithmic model for 9 BFD mixes.	171
Fig. 5.84	Relationship between deviator stress at failure and cell pressure for different curing periods	172
Fig. 5.85	Relationship between elastic modulus and cell pressure for different curing periods	172
Fig. 5.86	Modified failure envelopes at various curing periods for the optimum CSFD mix	173
Fig. 5.87	Relationship between deviator stress at failure and UCS	174
Fig. 5.88	Relationship between cohesion and UCS	175
Fig. 5.89	Scanning electron microscopy images of hydrated products of blast furnace slag-fly ash-dolime mixes for 1 day and 28 days of curing period.	177
Fig. 6.1	Grain size distribution curves of raw materials	180
Fig. 6.2	Modified Proctor compaction curves for various BC soil-dolime mixes	185
Fig. 6.3	Variation of UCS with dolime content for different curing periods	186
Fig. 6.4	Variation of UCS with curing period for different dolime contents	186
Fig. 6.5	Influence of deviatoric and confining stresses on resilient modulus of optimum BCD mix at 28 days curing	188
Fig. 6.6	Variation of resilient modulus with dolime contents for curing period of 28 days	189
Fig. 6.7	Effect of curing period on resilient modulus versus deviator stress relationship for optimum BCD mix and Granular Subbase (GSB) at a constant cell pressure of 34.5 kPa.	190
Fig. 6.8	Measured resilient modulus versus predicted resilient modulus using $M_r - \sigma_d$ model for 7 BCD mixes.	191
Fig. 6.9	Measured resilient modulus versus predicted resilient modulus using M_r - θ model for 7 BCD mixes.	192
Fig. 6.10	Measured resilient modulus versus predicted resilient modulus	192

using three parameter model for 7 BCD mixes

Fig. 6.11 Effect of curing period on permanent strain versus loading cycle relationship for optimum BCD mix and conventional Granular Subbase (GSB). 194

Fig. 6.12 Variation of permanent strain after 10000 cycles with dolime contents for 28 days of curing period. 194

Fig. 6.13 Measured plastic strain versus predicted plastic strain using logarithmic model for 7 BCD mixes. 195

Fig. 6.14 Relationship between deviator stress at failure and cell pressure for different curing periods 196

Fig. 6.15 Relationship between elastic modulus and cell pressure for different curing periods 197

Fig. 6.16 Modified failure envelopes at various curing periods for the optimum BCD mix and BC soil 198

Fig. 6.17 Relationship between deviator stress at failure and UCS 199

Fig. 6.18 Relationship between cohesion and UCS 199

Fig. 6.19 Scanning electron microscopy images of hydrated products of Black Cotton soil-dolime mixes for 1 day and 28 days of curing period. 201

Fig. 6.20 Modified Proctor compaction curves for different fly ash-dolime mixes 202

Fig. 6.21 Variation of UCS with dolime content for different curing periods 204

Fig. 6.22 Variation of UCS with curing period for different dolime contents 204

Fig. 6.23 Influence of deviatoric and confining stresses on resilient modulus of optimum FD mix at 28 days curing and GSB 206

Fig. 6.24 Variation of resilient modulus with dolime contents for curing period of 28 days 206

Fig. 6.25 Effect of curing period on resilient modulus versus deviator stress relationship for optimum FD mix and Granular Subbase (GSB) at a constant cell pressure of 34.5 kPa. 207

Fig. 6.26	Measured resilient modulus versus predicted resilient modulus using $M_r - \sigma_d$model for 7 FD mixes.	209
Fig. 6.27	Measured resilient modulus versus predicted resilient modulus using M_r - θ model for 7 FD mixes.	209
Fig. 6.28	Measured resilient modulus versus predicted resilient modulus using three parameter model for 7 FD mixes.	210
Fig. 6.29	Effect of curing period on permanent strain versus loading cycle relationship for optimum FD mix and conventional Granular Subbase (GSB).	211
Fig. 6.30	Variation of permanent strain after 10000 cycles with dolime contents for 28 days of curing period.	211
Fig. 6.31	Measured plastic strain versus predicted plastic strain using logarithmic model for 7 FD mixes.	213
Fig. 6.32	Relationship between deviator stress at failure and cell pressure for different curing periods	214
Fig. 6.33	Relationship between elastic modulus and cell pressure for different curing periods	214
Fig. 6.34	Modified failure envelopes of optimum FD mixes at various curing periods	215
Fig. 6.35	Relationship between deviator stress at failure and UCS	216
Fig. 6.36	Relationship between cohesion and UCS	216
Fig. 6.37	Scanning electron microscopy images of hydrated products of fly ash-dolime mixes for 1 day and 28 days of curing period.	218
Fig. 6.38	Variation of UCS with fly ash content for different curing periods	220
Fig. 6.39	Variation of UCS with curing period for different fly ash contents	221
Fig. 6.40	Influence of deviatoric and confining stresses on resilient modulus of optimum CF mix at 28 days curing and GSB	222
Fig. 6.41	Variation of resilient modulus with fly ash contents for curing period of 28 days	223
Fig. 6.42	Effect of curing period on resilient modulus versus deviator stress relationship for optimum CF mix and GSB at a constant cell	224

pressure of 34.5 kPa

Fig. 6.43 Measured resilient modulus versus predicted resilient modulus using $M_r - \sigma_d$model for seven CF mixes. 225

Fig. 6.44 Measured resilient modulus versus predicted resilient modulus using M_r - θ model for seven CF mixes. 226

Fig. 6.45 Measured resilient modulus versus predicted resilient modulus using three parameter model for seven CF mixes 226

Fig. 6.46 Effect of curing period on permanent strain versus loading cycle relationship for optimum CF mix and conventional Granular Subbase (GSB). 227

Fig. 6.47 Variation of permanent strain after 10000 cycles with fly ash contents for 28 days of curing period. 228

Fig. 6.48 Measured plastic strain versus predicted plastic strain using logarithmic model for 7 CF mixes 229

Fig. 6.49 Relationship between deviator stress at failure and cell pressure for different curing periods 230

Fig. 6.50 Relationship between elastic modulus and cell pressure for different curing periods 231

Fig. 6.51 Modified failure envelopes of optimum CF mixes at various curing periods 231

Fig. 6.52 Relationship between deviator stress at failure and UCS 232

Fig. 6.53 Relationship between cohesion and UCS` 233

Fig. 6.54 Scanning electron microscopy images of hydrated products of copper slag-fly ash mixes for 1 day and 28 days of curing period 234

Fig. 6.55 Modified Proctor compaction curves for various GBFS-fly ash mixes 236

Fig. 6.56 Variation of UCS with GBFS content and curing periods 237

Fig. 6.57 Influence of deviatoric and confining stresses on resilient modulus of optimum GBF mix at 28 days curing 238

Fig. 6.58 Variation of resilient modulus with GBFS contents for curing 239

period of 28 days

Fig. 6.59 Effect of curing period on resilient modulus versus deviator stress relationship for optimum GBF mix and GSB at a constant cell pressure of 34.5 kPa. 239

Fig. 6.60 Measured resilient modulus versus predicted resilient modulus using $M_r - \sigma_d$model for 7 GBF mixes. 241

Fig. 6.61 Measured resilient modulus versus predicted resilient modulus using M_r - θ model for 7 GBF mixes 241

Fig. 6.62 Measured resilient modulus versus predicted resilient modulus using three parameter model for 7 GBF mixes 242

Fig. 6.63 Effect of curing period on permanent strain versus loading cycle relationship for optimum GBF mix and conventional Granular Subbase (GSB). 243

Fig. 6.64 Variation of permanent strain after 10000 cycles with GBFS contents for 28 days of curing period 243

Fig. 6.65 Measured plastic strain versus predicted plastic strain using logarithmic model for 7 GBF mixes. 244

Fig. 6.66 Relationship between deviator stress at failure and cell pressure for different curing periods 245

Fig. 6.67 Relationship between elastic modulus and cell pressure for different curing periods 246

Fig. 6.68 Modified failure envelopes of optimum GBF mix at various curing periods 247

Fig. 6.69 Relationship between deviator stress at failure and UCS 248

Fig. 6.70 Relationship between cohesion and UCS 248

Fig. 6.71 Scanning electron microscopy images of hydrated products of GBFS-fly ash mixes for 1 day and 28 days of curing period. 250

Fig. 7.1 Particle size distribution of optimum slag-fly ash-dolime mixes and wet mix macadam (WMM). 252

Fig. 7.2 Modified Proctor compaction curves for different optimum mixes 253

Fig. 7.3	Variation of UCS with curing period for different optimum mixes	254
Fig. 7.4	Comparison ofdeviator stresses at failure for WMM and different optimum mixes after 28 days of curing period	255
Fig. 7.5	Comparison of elastic modulus for WMM and different optimum mixes after 28 days of curing period	256
Fig. 7.6	Influence of deviatoric stress on resilient modulus of optimum mixes after 28 days curing and WMM	258
Fig. 7.7	Effect of cell pressure on resilient modulus versus curing period relationship for optimum mixes at a constant deviatoric stress of 93.1 kPa	259
Fig. 7.8	Comparison of different models for prediction of resilient modulus of CFD mix for 28 days curing period	260
Fig. 7.9	Effect of curing period on permanent strain versus loading cycle relationship for optimum mixes and WMM	262
Fig. 7.10	Measured plastic strain versus predicted plastic strain using logarithmic model for optimum mixes	262
Fig. 7.11	Load-settlement curves for different optimum mixes and WMM	264
Fig. 7.12	Variation of vertical compressive strain at the top of subgrade with thickness of base layer for subgrade CBR of 4%.	266
Fig. 7.13	Variation of horizontal tensile strain at the bottom of bituminous (DBM) layer with thickness of base layerfor subgrade CBR of 4%.	266
Fig. 7.14	Plastic points developed in the pavement with optimum mixes and the pavement with WMM as base course at the same value of applied stress (= 575 kPa).	268
Fig. 7.15	Vertical compressive stress contour and vertical compressive strain contour developed within the pavement with optimum mixes and WMM as base course at the same value of applied stress (= 575 kPa)	269
Fig. 7.16	Variation of equivalent thickness of optimum mixes with WMM thickness for subgrade CBR of 4%.	270
Fig. 7.17	Particle size distribution of optimum mixes and granular subbase	273

Fig. 7.18	Modified Proctor compaction curves for different optimum mixes	274
Fig. 7.19	Variation of UCS with curing period for different optimum mixes	275
Fig. 7.20	Comparison of deviator stresses at failure for GSB, river bed material (RBM), coarse sand and different optimum mixes after 28 days of curing period	277
Fig. 7.21	Comparison of elastic modulus for GSB, river bed material (RBM), coarse sand and different optimum mixes after 28 days of curing period	277
Fig. 7.22	Influence of deviatoric stress and confining stress on resilient modulus of optimum mixes after 28 days curing and GSB	279
Fig. 7.23	Effect of curing period on resilient modulus of optimum mixes at a constant deviatoric stress and cell pressure	280
Fig. 7.24	Comparison of different models for prediction of resilient modulus of BCD mix for 28 days of curing period	281
Fig. 7.25	Effect of curing period on permanent strain versus loading cycle relationship for optimum mixes and GSB	283
Fig. 7.26	Measured plastic strain versus predicted plastic strain using logarithmic model for optimum mixes and GSB	284
Fig. 7.27	Load-settlement curves for different optimum mixes and GSB	285
Fig. 7.28	Variation of vertical compressive strain at the top of subgrade with thickness of subbase layer for subgrade CBR of 3%	287
Fig. 7.29	Variation of vertical compressive strain at the top of subgrade with thickness of subbase layer for subgrade CBR of 4%.	287
Fig. 7.30	Variation of horizontal tensile strain at the bottom of bituminous (DBM) layer with thickness of subbaselayerfor subgrade CBR of 3%.	288
Fig. 7.31	Variation of horizontal tensile strain at the bottom of bituminous (DBM) layer with thickness of subbaselayerfor subgrade CBR of 4%	288
Fig. 7.32	Plastic points developed in the pavement with optimum mixes and GSB as subbase course for subgrade CBR of 3% at same value of	289

applied stress (= 575 kPa)

Fig. 7.33 Vertical compressive stress contour and vertical compressive strain contour developed within the pavement with optimum mixes and GSB as subbase course for subgrade CBR of 3% at the same value of applied stress (= 575 kPa) 290

Fig. 7.34 Variation of equivalent thickness of optimum mixes with GSB thickness for subgrade CBR of 3% 292

Fig. 7.35 Variation of equivalent thickness of optimum mixes with GSB thickness for subgrade CBR of 4% 292

List of Tables

Table No.	Description	Page No.
Table 1.1	Local and waste materials for road construction	2
Table 1.2	Chemical composition of the copper slag	6
Table 1.3	Steel production in different countries in 2007	7
Table 1.4	Chemical composition of electric arc furnace slag	9
Table 1.5	Chemical composition of blast furnace slag	10
Table 1.6	Chemical composition of Dolime	11
Table 2.1	Summary of literature related to the properties of copper slag and its utilization	22
Table 2.2	Results of UCS tests on copper slag (75%) + fly ash (25%) mixes with different cement content	25
Table 2.3	Summary of literature related to the properties of steel slag and its utilization	27
Table 2.4	Test results for blast furnace slag and steel slag	28
Table 2.5	CBR and UCS test results of selected mixes	28
Table 2.6	Reactivity of steel slags	31
Table 2.7	Summary of literature related to the properties of blast furnace slag and its utilization	32
Table 2.8	CBR of different admixtures	33
Table 2.9	Elastic modulus of test sections from plate load test at 1.5 mm deflection	34
Table 2.10	Unconfined compressive strength (kPa) for 7 days curing	35
Table 2.11	CBR value of stabilized mixes (after 7 days curing)	35
Table 2.12	CBR and triaxial test results	36
Table 2.13	MDD and OMC for BF Slag-fly ash mixes	36
Table 2.14	Summary of literature related to the properties of lime stabilized expansive soil and its utilization	38
Table 2.15	Results of consistency limits and Free Swell Index	41

Table 2.16	Results of CBR and UCS test	43
Table 2.17	Summary of literature related to the dynamic behavior of conventional and waste materials	45
Table 2.18	CBR and E-Values	49
Table 2.19	Values of K_1 and K_2 for different materials	52
Table 3.1	Proportions of different raw materials in CSFD and BFD trial mixes	62
Table 3.2	Loading sequences used in repeated load triaxial testing as per AASHTO T 307- 2000	64
Table 5.1	Physical properties of the raw materials	78
Table 5.2	Chemical composition of the raw materials in percentage by weight	79
Table 5.3	Leaching test results of the raw materials	80
Table 5.4	Model constants of CFD mixes for a given fly ash content	91
Table 5.5	Model constants for different mix proportions of copper slag-fly ash-Dolime for 28 days of curing period	98
Table 5.6	Model constants of optimum CFD mix for different curing period and for conventional Wet Mix Macadam (WMM)	98
Table 5.7	Model constants for different CFD mix proportions for 28 days of curing period	104
Table 5.8	Model constants of optimum CFD mix for different curing period and for conventional Wet Mix Macadam (WMM)	105
Table 5.9	Total strength parameters of optimum CFD mix (80C-20F-15D) after different curing periods	110
Table 5.10	X-ray diffraction peaks intensity for various hydration products of Dolime, fly ash and CFD mixes.	113
Table 5.11	Model constants of FSFD mixes for a given fly ash content	122
Table 5.12	Model constants for different mix proportions of fine steel slag-fly ash-Dolime for 28 days of curing period	126
Table 5.13	Model constants of optimum FSFD mix for different curing period	126
Table 5.14	Model constants for different FSFD mixes for 28 days of curing period	131

Table 5.15	Model constants of optimum FSFD mix for different curing period	131
Table 5.16	Total strength parameters of optimum FSFD mix (75S-25F-15D) after different curing periods	135
Table 5.17	X-ray diffraction peak intensity for various compounds of Dolime, fly ash and FSFD mixes.	137
Table 5.18	Physical properties of different trial CSFD mixes	140
Table 5.19	Model constants for different mix proportions of coarse steel slag-fly ash-dolime for 28 days of curing period	147
Table 5.20	Model constants of optimum CSFD mix for different curing period	147
Table 5.21	Model constants for different CSFD mixes for 28 days of curing period	151
Table 5.22	Model constants of optimum CSFD mix for different curing period	151
Table 5.23	Total strength parameters of optimum CSFD mix after different curing periods	155
Table 5.24	X-ray diffraction peak intensity for various compounds of dolime, fly ash and CSFD mixes.	157
Table 5.25	Physical properties of different trial BFD mixes	159
Table 5.26	Model constants for different mix proportions of blast furnace slag-fly ash-Dolime for 28 days of curing period	165
Table 5.27	Model constants of optimum BFD mix for different curing period	166
Table 5.28	constants for different BFD mixes for 28 days of curing period	170
Table 5.29	constants of optimum BFD mix for different curing period	170
Table 5.30	Total strength parameters of optimum BFD mix after different curing periods	173
Table 5.31	X-ray diffraction peak intensity for various compounds of Dolime, fly ash and BFD mixes.	176
Table 6.1	Physical properties of the raw materials	180
Table 6.2	Chemical composition of the raw materials in percentage by	181

	weight	
Table 6.3	Leaching test results of the raw materials	182
Table 6.4	Atterberg limits and free swell index of BC soil-dolime mixes	183
Table 6.5	Soaked CBR values for BC soil-dolime mixes	187
Table 6.6	constants for different BCD mixes and GSB	191
Table 6.7	Model constants for different BCD mixes and GSB	195
Table 6.8	Total strength parameters of optimum BCD mix after different curing periods	198
Table 6.9	X-ray diffraction peak intensity (counts per second) for various compounds of dolime, BC soil and BCD mixes.	200
Table 6.10	Soaked CBR values of fly ash and fly ash-dolime mixes	205
Table 6.11	Model constants for different FD mixes	208
Table 6.12	Model constants for different FD mixes	212
Table 6.13	Total strength parameters of optimum FD mix after different curing periods	215
Table 6.14	X-ray diffraction peak intensity (counts per second) for various compounds of dolime, fly ash and FD mixes.	217
Table 6.15	Soaked CBR values of optimum CF mix	221
Table 6.16	Model constants for different CF mixes	225
Table 6.17	Model constants for different CF mixes	229
Table 6.18	Total strength parameters of optimum CF mix after different curing periods	232
Table 6.19	X-ray diffraction peak intensity (counts per second) for various compounds of fly ash and CF mixes.	234
Table 6.20	Soaked CBR values of different GBF mixes	236
Table 6.21	Model constants for different GBF mixes	240
Table 6.22	Model constants for different GBF mixes	244
Table 6.23	Total strength parameters of optimum GBF mix after different curing periods	247
Table 6.24	X-ray diffraction peak intensity (counts per second) for various compounds of fly ash and GBF mixes.	249

LIST OF NOTATIONS

ϕ	Angle of friction
P_a	Atmospheric pressure
θ	Bulk stress
C_c	Coefficient of curvature
R^2	Coefficient of determination
c	Cohesion of soil
σ_3	Confining pressure
T	Curing period in days
σ_d	Deviator stress
R_i	Resistance index
σ_1	Major principal stress
δ	Maximum deformation on the pavement surface
ε_t	Horizontal tensile strain
a, b, c, k_1, k_2, k_3, k_4, k_5, k_6 and k_7	Model constants
E	Modulus of elasticity
ε_p	Permanent strain
D_r	Relative density
ε_r	Resilient (elastic) strain
M_r	Resilient modulus
t	Thickness
q_u	Unconfined compressive strength
C_u	Uniformity coefficient
ε_v	Vertical compressive strain

LIST OF ABBREVIATIONS

AASHTO	American association of state highway and transportation officials
ASTM	American society for testing and materials
BC soil	Black Cotton soil
BC layer	Bituminous concrete layer
BCD	Black Cotton soil-dolime
BCS	Blended calcium sulphate
BF	Blast furnace
BFD	Blast furnace slag-fly ash-dolime
BFS	Blast furnace slag
BOF	Basic oxygen furnace
C-A-S-H	Calcium aluminosilicate hydrate
CBR	California bearing ratio
CF	Copper slag-fly ash
CFD	Copper slag-fly ash-dolime
CSFD	Coarse steel slag-fly ash-dolime
C-S-H	Calcium-silicate-hydrate
CSM	Conventional Sub base Materials
D	Dolime
DBM	Dense bituminous macadam
DGS	Densely graded steel slag
EAF	Electric arc furnace
F	Fly ash
FA	Foamed asphalt

FAUP	Flyash utilization programme
FD	Fly ash-dolime
FSFD	Fine steel slag-fly ash-dolime
FSI	Free swell index
FWD	Falling weight deflectometer
GBF	Granulated blast furnace slag-fly ash
GBFS	Granulated blast furnace slag
GSB	Granular Sub base
GW	Well graded gravel
IRC	Indian roads congress
IS	Indian standards
kN	Kilo Newton
kPa	Kilo Pascal
LD	Linz-donawitz
LL	Liquid limit
LVDT	Linear Variable differential transformer
MDD	Maximum dry density
MDR	Major district road
ML	Low compressible silt
MPa	Mega Pascal
NH	National highway
NHDP	National highway development programme
OMC	Optimum moisture content
PI	Plasticity index
PL	Plastic limit

PMGSY	Pradhan mantri gram sadak yojna
RAP	Reclaimed asphalt pavement
RBM	River bed material
RLT	Repeated load triaxial
RSS	Residual sum of squares
SEM	Scanning electron microscopy
SH	State highway
SLR	Service life ratio
SM	Silty sand
SN	Structural number
SP	Poorly graded sand
SSA	Steel slag aggregate
SVNIT	SardarVallabhbhai National Institute of Technology
SW	Well-graded sand
TCLP	Toxicity characteristic leaching procedure
UCS	Unconfined compressive strength
USA	United States of America
UU	Unconsolidated undrained
WAS	West African standard
WBM	Water bound macadam
WMM	Wet mix macadam
XRD	X-ray diffraction